Ferromagnetic ordering in THAB exfoliated WS2 nanosheet

Article in Journal of Physics D: Applied Physics · March 2021 DOI: 10.1088/1361-6463/abe331 CITATIONS READS 190 11 4 authors, including: Bikash Shaw Anup Debnath Pachhunga University College University of Cambridge 19 PUBLICATIONS 229 CITATIONS 40 PUBLICATIONS 1,001 CITATIONS SEE PROFILE SEE PROFILE Shatabda Bhattacharya Czech Academy of Sciences, Institute of Physics 31 PUBLICATIONS 462 CITATIONS SEE PROFILE

PAPER

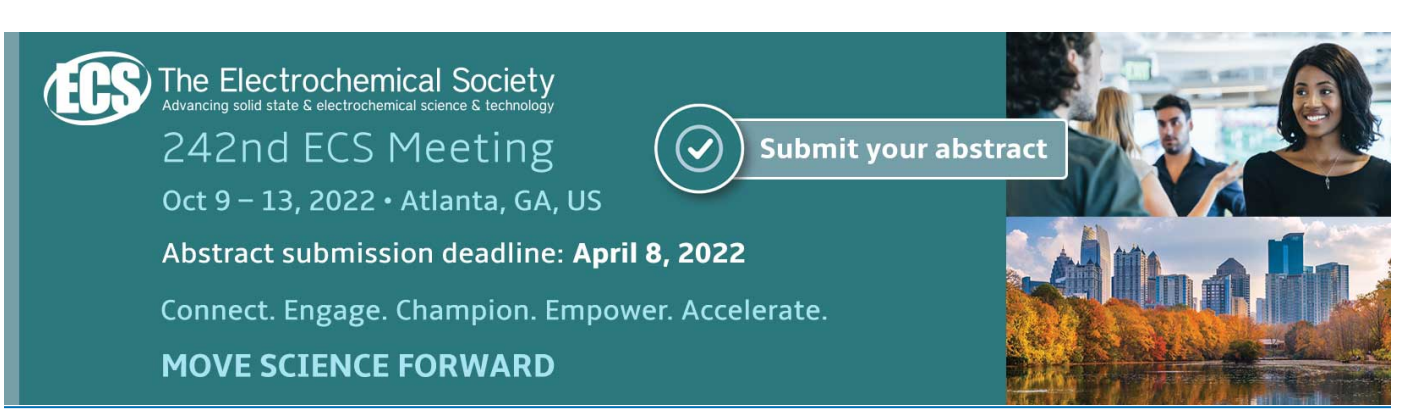
Ferromagnetic ordering in a THAB exfoliated WS₂ nanosheet

To cite this article: Anup Debnath et al 2021 J. Phys. D: Appl. Phys. 54 205001

View the article online for updates and enhancements.

You may also like

- Immittance Model of Anodic Dissolution of Ferromagnetic Materials
 Elena A. Baranova and Oleksandr Kuznetsov
- Anisotropic Magnetoresistance of Ferromagnetic Conductive Filament in Resistive Switching Memory Shintaro Otsuka, Yoshifumi Hamada, Tomohiro Shimizu et al.
- GaN-Based Dilute Magnetic Semiconductors for Room Temperature Neuromorphic and Quantum Computing Chuanle Zhou, Amirhossein Ghods, Vishal G. Saravade et al.



J. Phys. D: Appl. Phys. 54 (2021) 205001 (12pp)

https://doi.org/10.1088/1361-6463/abe331

Ferromagnetic ordering in a THAB exfoliated WS₂ nanosheet

Anup Debnath¹, Bikash Kumar Shaw², Shatabda Bhattacharya³ and Shyamal K Saha^{1,*}

E-mail: cnssks@iacs.res.in

Received 12 December 2020, revised 9 January 2021 Accepted for publication 4 February 2021 Published 1 March 2021



Abstract

Because of the important role of two-dimensional (2D) magnetic semiconductors in low-dimensional spintronic devices, the generation of ferromagnetism within an ultrathin semiconducting sheet of a transition metal dichalcogenide is highly desirable. A pristine WS₂ sheet is a diamagnetic semiconducting transition metal dichalcogenide with superior electronic properties. In this study, we synthesised a free-standing WS₂ sheet by a chemical route followed by electrochemical exfoliation by a giant molecule. During exfoliation of the WS₂ crystal, atomic vacancies were created in the sheet with a lower number of layers. To understand the mechanism of exfoliation, we carried out x-ray diffraction, transmission electron microscopy, atomic force microscopy and Raman measurements. The types of atomic vacancies were realised by energy-dispersive x-ray spectroscopy, high-resolution transmission electron microscopy (fast Fourier transform), and x-ray photoelectron spectroscopy studies. We also observed a ferromagnetic ordering within the exfoliated WS₂ sheet, which is explained on the basis of the generation of an atomic vacancy induced spin-moment. The transport study of the exfoliated WS₂ sheet suggests that the electro-transport behaviour still remains as a semiconductor even after exfoliation. This ferromagnetic semiconducting system will be applicable in spintronic devices and this technique will enrich the literature, particularly for the preparation of a 2D semiconducting ferromagnet in a facile fashion.

Supplementary material for this article is available online

Keywords: WS₂, 2D ferromagnet, electrochemical-exfoliation, THAB intercalation, Mott-VRH, spintronic-material

1

(Some figures may appear in colour only in the online journal)

1. Introduction

Transition metal dichalcogenides (TMDs) such as WS₂, MoS₂, WSe₂, MoSe₂, WTe₂, MoTe₂, etc, in their twodimensional (2D) form, have received great attention in

* Author to whom any correspondence should be addressed.

the fields of electronics, optoelectronics, and especially spintronics due to their unique features (e.g. strong spin-orbit coupling, large spin-relaxation length and breaking-inversion symmetry for monolayer), depending on their thickness [1–3]. Like other TMDs, WS₂ also has a layer-type structure, having a strong in-plane bonding (W–S covalent bond) and a weak out-of-plane bonding (van der Waals interaction), with

¹ School of Materials Sciences, Indian Association for the Cultivation of Science, Jadavpur, Kolkata 700032, India

² Department of Materials Science and Metallurgy, University of Cambridge, Cambridge CB3 0FS, United Kingdom

³ National Creative Research Initiative Centre for Spin Dynamics & Spin-Wave Devices, Nanospinics Lab, Department of Materials Science and Engineering, Seoul National University, Seoul 08826, Republic of Korea

a honeycomb plane of W (metal) atoms sandwiched between two similar planes of S (chalcogen) atoms [1]. Many methods, such as annealing [4], mechanical exfoliation [5], wet chemical approach [6], physical vapour deposition [7], and sulphurisation of transition metal films [8], are available in the literature for the successful synthesis of a thin layer of other TMDs (MoS₂, MoSe₂, MoTe₂, etc). However, due to the tendency of WS₂ to form a closed fullerene-like structure [9], stackedmultilayer [10] or nanotube-like structure [10, 11], synthesis techniques for a 2D WS₂ sheet are limited. In addition, because of the thermodynamic instability of a thin layer (below a dozen layers) of WS₂, it is indeed a real challenge to achieve a freestanding ultrathin layer of WS₂ [12]. Therefore, to realise a freestanding, good quality and thin layer of WS2 sheet, exfoliation of its bulk crystal by the method of intercalation of smallradius alkali ions (e.g. Li⁺, Na⁺, etc) within the van der Waals gap of the crystal might be a good approach. But there would be an undesired phase transformation (from 2H-WS2 to 1T-WS₂) [13, 14]. As the size of the Li⁺ (or Na⁺) ion is very small, in this process of exfoliation by intercalation of a Li⁺ (or Na⁺) ion, a huge number of ions is needed to be intercalated within the host (WS2) crystal to form a large amount of Li_xWS₂ complex. The detailed mechanism, along with the drawbacks of the process of the intercalation of an alkali metal ion and the exfoliation of TMDs (MoS₂ or WS₂), are discussed in the supplementary material. In a particular TMD (e.g. WS₂), number of electrons in the d orbitals of the transition metal (W) determine the electronic structure of that TMD (WS₂). In all TMDs, the transition metals have an oxidation state of +4and that of the chalcogens is -2. Thus, in WS₂, the number of electrons in the d-orbital of W is 2 and the system (d²) shows trigonal prismatic coordination. During the formation of the Li_xWS₂ complex in the Li⁺ ion intercalation of the WS₂ crystal as described above, electron transfer occurs from Li to W, and the d² system changes to d³. Due to this electron transfer, metal coordination is changed from trigonal prismatic geometry to octahedral geometry, which results in the change in crystal structure from 2H-WS₂ to 1T-WS₂ [13, 14]. In 2H-WS₂ there is a bandgap between the occupied d_z² band and unoccupied $d_x^2 - y^2$, xy, and it shows a semiconducting nature. However, in 1T-WS2, due to the extra electron within the metal d orbitals, degeneracy (dxy,yz,xz) occurs and the Fermi level resides at the middle of the single degenerate band, and the crystal shows metallic behaviour [6, 13, 14]. To overcome this problem, a two-step synthesis method was followed. In this study, first, a 2D sheet of WS₂ crystal was synthesised using a wet-chemical approach [15, 16]. Then the sheet was exfoliated using the approach of electrochemical-intercalation of a giant molecule (tetraheptylammonium bromide) within the crystal. As the molecular size of the tetraheptylammonium ion is very large, only a few ions intercalated within the WS2 crystal are needed for exfoliation. As a result, this method of exfoliation of a 2D TMD (WS₂) is completely free from the problem of phase-transformation mentioned earlier [17, 18].

It is known that a ferromagnetic semiconductor can ideally generate and detect tunable spin-current, which is the essential property that is required in an ideal spintronic device [19]. Like other TMDs (MoS₂, MoSe₂, etc), a single layer of pristine WS₂ is intrinsically a diamagnetic, direct band-gap semiconductor [20]. Therefore, to be useful in spintronic devices, it is essential to invoke ferromagnetism in the 2D WS₂ sheet. It was reported that, in 2D TMDs (e.g. MoS₂), atomic vacancies play a pivotal role to generate a magnetism within the system [21, 22]. Earlier theoretical studies suggested that point defects in 2D TMDs (e.g. WS₂) are created in two different fashions: atomic vacancy defects and antisite defects [23, 24]. In atomic vacancy defects one or more than one S or W atom(s) are missing individually or together. The common atomic vacancies are V_{1S} (one atom is missing in the S site), V_{2S} (two atoms are missing in the S site), V_{6S} (six atoms are missing in the S site), V_{1W} (one atom is missing in the W site), V_{1W+1S} (one W atom along with one S atom are missing) and V_{1W+2S} (one W atom along with two S atoms are missing). In the antisite defect, one or more than one S atom(s) replace(s) one or more than one W atom(s) and vice versa. The common antisites are S_{1W} (one S atom replaces one W atom), S2_{1W} (two S atoms replace one W atom), W1S (one W atom replaces one S atom), and W2_{2S} (two W atoms replace two S atoms). The ordering of the formation energy (ΔE) for all the atomic vacancy defect and antisites are $V_{1S} < V_{2S} < V_{1W} < S_{1W} < S_{2W} < W_{1S} < W_{2S}$ [23]. This indicates that the antisites are formed at higher temperature (>1100 °C) whereas the atomic vacancies are created in a low energy value. Atomic vacancy defects such as V_{6S} , V_{3W} and V_{1W+2S} vacancies introduced in a layer of WS2 generate a significant amount of magnetic moment, whereas the same for V_{1S} , V_{2S} , V_{1W} and V_{1W+1S} do not generate any magnetism in the system [24, 25]. The amount of total spin magnetic moments generated, due to the V_{1W+2S} atomic vacancy, V_{6S} atomic vacancy and V_{3W} atomic vacancy, are 0.981, 0.608 and 0.169 μ_B , respectively [25]. This magnetic moment is generated as a result of the exchange interaction between S p-states and W d-states near the vacancy defects [25]. Using different characterisation techniques, the defect states have been estimated for the as-prepared WS2 samples. On exfoliation of the WS2 sheet, the intrinsic structural vacancy defects come into play in the electrochemically exfoliated WS2 layers and ordering of magnetic moment is observed [26, 27]. As a result of this, a net magnetisation has been generated within the system. This type of ferromagnetic ordering is limited and is destroyed with the rise in temperature. The proper exfoliation of the sheet plays a key role in the observed magnetism. As the electrochemicalintercalation time for the exfoliation increases, the better saturation of magnetisation with fairly good coercivity (1227 Oe at 2 K) in the magnetic result is observed. The electrical measurement confirms the semiconducting behaviour of the WS₂ sheet even after the electrochemical exfoliation which makes it useful for spintronic applications. This finding can enrich the literature about 2D ferromagnetic semiconductors and the as-prepared ferromagnetic semiconductor (WS2 system) with moderate magnetic moment will be very useful in spintronic devices.

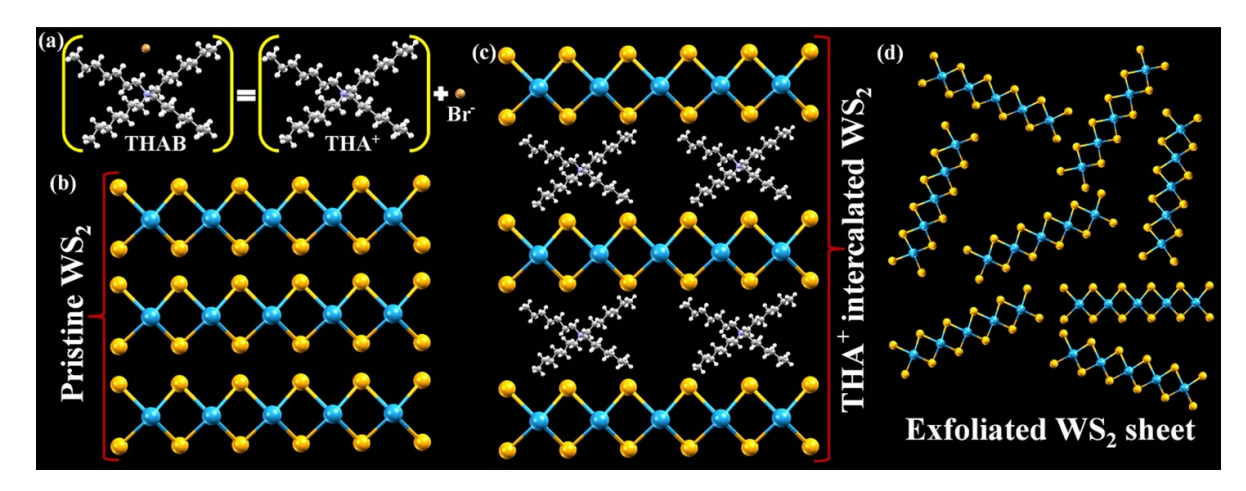


Figure 1. Schematic diagram of (a) ionisation of THAB, (b) layer structure of WS_2 , (c) THA⁺ intercalated WS_2 layers and (d) exfoliated WS_2 sheets.

2. Experimental section

2.1. Chemicals used

Tetraheptylammonium bromide (THAB) [[CH₃(CH₂)₆]₄N(Br)] (99%, Sigma-Aldrich), acetonitrile (99.8%, Sigma-Aldrich), 1-octadecene (90%, Merck), oleylamine (70%, Sigma-Aldrich), acetone (99%, Merck), n-hexane (95%, Sigma-Aldrich), ethanol (99.99%, Merck), thiourea [(NH)₄CS] (99%, Sigma-Aldrich), and tungsten (VI) chloride [WCl₆] (99.99%, Sigma-Aldrich) were purchased and used without further purification.

2.2. Chemical synthesis

The molecular thick WS₂ layer was synthesised using a unique two-step synthesis technique. In the first step, WS₂ crystal was synthesised by using a facile colloidal synthesis route [15, 16]. Then the WS₂ crystal was exfoliated by using the method of electrochemical exfoliation [17, 18]. For the chemical synthesis, thiourea was crushed as a fine powder in a mortar and pestle set. One hundred and fifty-four mg of such thiourea powder was dispersed in 10 ml of oleylamine by ultrasonication, followed by stirring, and taken in a 20 ml beaker under an Argon-atmosphere. Meanwhile, in a 50 ml RB flux, 396 mg of WCl6 was added to 20 ml of oleylamine. The mixture was then degassed by pure argon for 30 min and the temperature was raised to 70 °C. After adding 5 ml of 1-octadecene, we maintained the fixed temperature for 15 min. Then the previously prepared solution of thiourea was injected and the temperature was raised to 280 °C and maintained for 4 h. As the temperature of the reaction medium changed from 70 °C to 280 °C, the colour of the reacting solution changed to black. After 4 h refluxing, we allowed the reaction chamber to cool to room temperature. After reaching room temperature, 15 ml of n-hexane and 15 ml of a mixture of ethanol and acetone were added to the black-coloured yield and allowed to get precipitated overnight in an unstirred condition. The precipitation was washed with a mixture of n-hexane, ethanol and acetone (volume ratio of 1:1:2) several times to remove the organic solvents and other unreacted molecules. In the end, the final black coloured product was dried in a vacuum oven at $65\,^{\circ}\text{C}$ for $10\,\text{h}$ and the WS₂ polycrystalline powder sample was collected.

2.3. Electrochemical exfoliation

In the second step, we exfoliated the WS₂ sheet by intercalation of a giant molecule (THAB) using the method of electrolysis [17, 18]. To perform the electrolysis, we prepared the electrolyte solution by dissolving 200 mg THAB in 40 ml acetonitrile. The WS2 was used as a cathode and a glassy carbon electrode was used as an anode and a 9-volt battery was connected to perform the electrolysis (see figure S1 of the supplementary material (available online at stacks.iop.org/JPD/54/205001/mmedia)). The detailed experimental setup and step-by-step demonstration of the electrolysis process are described in the supplementary material. Figure 1 shows a schematic representation of the intercalation process. In the electrolytic solution, THAB, i.e. [CH₃(CH₂)₆]₄N(Br), molecules get separated as THA⁺ ([CH₃(CH₂)₆]₄N⁺) and Br⁻ (figure 1(a)). During the electrolysis, THA+ ions are inserted within the WS2 sheet (figures 1(b)-(c)) which take an electron from the external circuit to achieve charge neutrality and Br- releases an electron to the anode and Br₂ (yellow-coloured suspension) accumulates near the anode (see figure S1(c) of the supplementary material). The electrochemical reaction is as follows:

$$THAB \rightarrow THA^{+} + Br^{-}$$

$$WS_2 + xTHA^+ + xe^- \text{ (cathode)} \rightarrow (THA^+)_x WS_2^{x-}$$

$$x\mathrm{Br}^- \to \frac{x}{2}\mathrm{Br}_2 + x\mathrm{e}^- \text{ (anode)}.$$

As time went on, the spreading of the yellow-coloured suspension throughout the whole solution indicated a greater amount of Br_2 release in the solution and a greater amount of intercalation of the THA^+ ion within the WS_2 crystal. As a result of this intercalation, the volume of the WS_2

crystal increased and it became fluffy (see figure S1(d) in the supplementary material). To collect the fluffy WS $_2$ crystal, ethanol and acetone were added to it and ultrasonication was performed for 4 h. During the ultrasonication, exfoliation of the WS $_2$ sheet took place from the THA $^+$ -intercalated fluffy WS $_2$ crystal (figure 1(d)). The exfoliated WS $_2$ sheet was washed by ethanol and acetone several times and collected after drying in a vacuum oven at 60 °C for 9 h. We prepared three different samples, WS $_2$ -1h, WS $_2$ -2h and WS $_2$ -10h, for three different electrolysis times (1, 2 and 10 h, respectively), keeping the other conditions same.

2.4. Characterisation

The microstructure, morphology and energy-dispersive x-ray spectroscopy (EDXS) of the samples were characterised using a JEOL-2011 high-resolution transmission electron microscope (HRTEM). The Raman spectroscopy was performed using a triple Raman spectrometer ($\lambda = 532 \text{ nm}$) by HORIBA Scientific (model no. T64000). To confirm the intercalation within the WS₂ crystal and for phase confirmation, we carried out powder x-ray diffraction (PXRD) measurement of the samples. The PXRD measurements were carried out at an interval of 2 s for $2\theta \sim 0.01^{\circ}$ within the range from 10° to 80°, in an advanced diffractometer from RIGAKU SMART LAB-XRD ($\lambda = 1.54$ Å of Cu–K $_{\alpha}$ line). The thicknesses of the as-prepared samples was measured using atomic force microscopy (AFM) by Oxford Instruments (Asylum Research MFP-3D Origin). AFM measurement was performed of the sample mounted on a silicon wafer in a spin coating system from Apex Instruments (model no. spinNXG-P1). The x-ray photoelectron spectroscopy (XPS) was done using a monochromatic Al K_{α} line in an XPS measurement system from Omicron Nanotechnology. The transportation measurements were performed using a Keithley 6514 electrometer and a Cryogenics cryostat in a high vacuum condition. The magnetic measurements were carried out in a superconducting quantum interference device (SQUID), model no. MPMS XL 5 made by Quantum Design (USA).

3. Results and discussion

3.1. TEM image analysis

Figures 2(a) and (c) show the overall TEM image, the selected area electron diffraction pattern (SAED), and the HRTEM image, respectively, for the chemically synthesised WS₂ sheet. The lattice parameter of 2.7 Å calculated from the SAED pattern confirms the (100) plane of WS₂ crystal [28, 29]. To understand the phase purity of the as-synthesised single crystal or presence of any defect or dislocation of the crystal, fast Fourier transform (FFT) and inverse fast Fourier transform (IFFT) were calculated from the HRTEM image of the chemically synthesised WS₂. Figures 2(d) and (e) show the FFT and IFFT, respectively. From the IFFT, it is clear that there are no defects or Moiré pattern-like decoration within the crystal. From the digital image (TEM image) micrograph of the THA⁺ intercalated WS₂ sample, as shown in figure 2(f),

it is clear that, due to the intercalation of the giant molecules within the interlayer separation of the WS₂ sheet, it gets ruptured and fluffy but the electrolysis is not sufficient enough to get a thin layered WS₂ crystal. To achieve a thin layer, it needs proper ultrasonication and sample collection, which is already discussed in the synthesis section. The TEM measurement for the final exfoliated sample was also performed. In the TEM image of the final sample (exfoliated sample), as shown in figure 2(g), there is a thin layer of WS₂ sheet. Figure 2(h) shows the SAED pattern of the sample, which indicates the good crystallinity and confirms the phase (lattice parameter of 2.7 Å for the (100) set of planes) of the WS₂ crystal. The corresponding HRTEM image for the sample is shown in figure 2(i). To know the lattice parameter and microdetail of the crystal, FFT of the HRTEM image was taken and is shown in the inset of figure 2(i). The corresponding IFFT calculated from the spots in the FFT is shown in figure 2(j). The lattice parameter of 2.7 Å in the IFFT confirms the (100) plane of the WS₂ crystal [28, 29]. In the IFFTs, there are many defects, and Moiré patterns of the exfoliated sheet are observed. These patterns indicate that the exfoliated crystal has got defect states and vacancies. In figure 2(k), the EDXS analysis for the sample represents the stoichiometry of the WS₂ crystal. From the elemental percentage, calculated from the EDXS data, we found that the elemental ratio of W to S in our sample is 1:1.83 instead of 1:2. This data suggests the significant number of atomic vacancies at the S site within the as-exfoliated WS2 sheet.

3.2. Raman spectra analysis

Figure 3(a) shows four Raman active modes $(A_{1g}, E_{2g}^1, E_{1g})$ and E_{2g}^2) of the WS₂ crystal [30, 31]. The A_{1g} mode is for the outof-plane vibration of two sulphur atoms in opposite directions and is very sensitive to the layer number or the thickness of the WS₂ sheet. The E_{2g}^1 mode is due to the in-plane vibration of two sulphur atoms in opposite to a tungsten atom in a particular layer and depends on the lateral dimension of the WS₂ crystal. The E_{1g} mode is due to the in-plane vibration of two sulphur atoms only, in opposite directions, and this mode is forbidden in a backscattering arrangement [30-32]. The E_{2g}^2 mode at a very low frequency range ($<50 \,\mathrm{cm}^{-1}$) is due to the vibration of two adjacent layers in opposite directions and obstructed by the experimental arrangement (notch filter of wavenumber $>100 \text{ cm}^{-1}$) [30, 31]. Figure 3(b) shows the Raman spectra for three exfoliated samples (WS2-1h, WS2-2h and WS₂-10h) along with the bare-WS₂ sample. Peak positions, difference between the peaks (Δ) and the intensity ratio for the peaks of the E_{2g}^1 and A_{1g} modes for all the samples are tabulated in table 1. It is seen that, as the electrolysis time is increased, the intensity of the A_{1g} mode (directly related to the layer number) decreases and a redshift (maximum 8.1 cm⁻¹ WS₂-10h) is observed. However, no significant change in the intensity of the E_{2g}^1 mode is observed along with a slight blueshift (maximum 1.1 cm⁻¹ for WS₂-10h). These results indicate the better exfoliation of the WS₂ crystal with the increase in electrolysis time. The intensity ratios $\left(I_{E_{2g}^1}/I_{A_{1g}}\right)$ for the bare-WS₂, WS₂-1h, WS₂-2h and

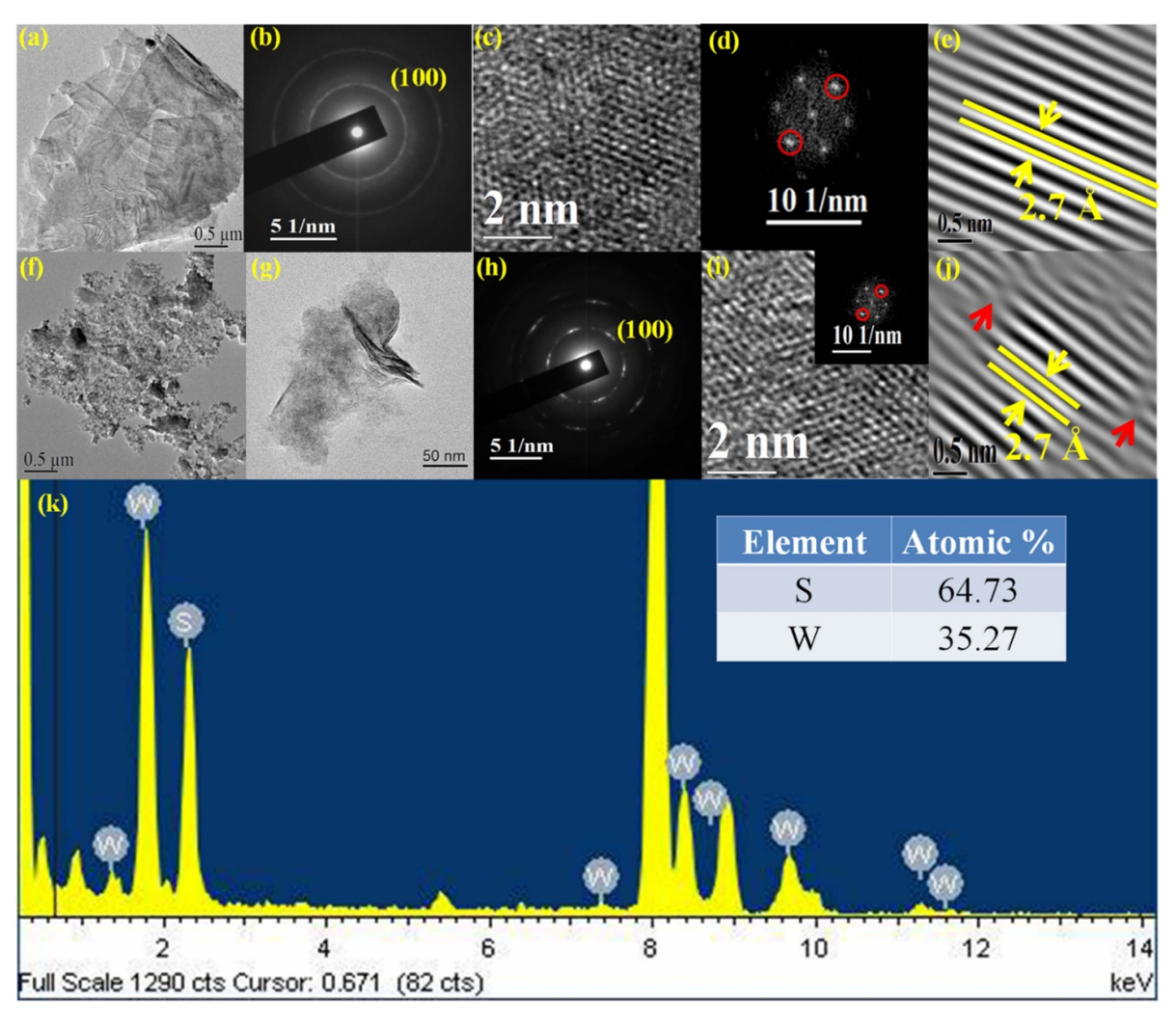


Figure 2. (a) TEM image of the chemically synthesised bare-WS $_2$ sheet, (b) SAED pattern of the bare-WS $_2$ sample, (c) HRTEM image of the bare-WS $_2$ sheet, (d) FFT obtained from HRTEM image of the bare-WS $_2$ sheet, (e) IFFT calculated from the FFT spots in panel (c), (f) TEM image of the THA $^+$ intercalated WS $_2$ sheet, (g) TEM image of the exfoliated WS $_2$ layer, (h) SAED pattern of the exfoliated WS $_2$ layer, (i) HRTEM image of the exfoliated WS $_2$ layer, and corresponding FFT (inset), (j) IFFTs calculated from the FFT spots in the inset of panel (i) and (k) EDXS analysis of the exfoliated WS $_2$ sample.

WS₂-10h samples are calculated as 1.06, 1.43, 1.55 and 2.61, respectively, whereas the differences (Δ) between the peak positions (E_{2g}^1 and A_{1g} modes) for these four samples become 71.8, 68.5, 67.1 and 63.7 cm⁻¹, respectively. This data indicates that, as the intercalation time increases, better exfoliation occurs and, as a result of this, the layer number in the asexfoliated sheet becomes less [30–32]. As the intensity ratio ($I_{E_{2g}^1}/I_{A_{1g}}$) is the maximum, and the difference between the peak positions (Δ) is the minimum for the WS₂-10h sample, it can be concluded that there is a minimum number of layers in the sheet of the WS₂-10h sample. However, the exact layer number in a particular sheet has been calculated by using AFM and TEM data. The details of the calculation are discussed in a later section.

3.3. PXRD analysis

Figure 4(a) shows the PXRD pattern in the low angle region $(5^{\circ}-30^{\circ})$ for the as-synthesised bare-WS₂ sample and the

THA+ intercalated WS2 sample (for a full range plot, see figure S2 in the supplementary material). Four additional peaks apart from the original peak (14.15°) for the (002) set of planes of the bare-WS2 crystal are observed in the case of the intercalated WS2 sample. From the Rietveld refinement [33–35], we have indexed these four additional peaks at 6.30° , 12.63° , 19.00° and 25.42° , as a (002), (004), (006), (008) set of planes, respectively (figure 4(a)). A detailed description of the Rietveld refinement is discussed in the supplementary material. The shifting (towards the lower angle) of the peak position for the (002) set of planes indicates the larger van der Waals gap between two adjacent layers, i.e. the intercalation of THA^+ ions [17, 18, 36]. The other peak positions at the higher angle region are almost at the same positions, which indicates the absence of any new generated phase (see figure S2 in the supplementary material). Figure 4(b) shows the PXRD pattern for three exfoliated samples (WS₂-1h, WS₂-2h and WS₂-10h) along with the bare-WS2 sample. From the Rietveld refinement, we confirmed the 2H-phase (space group: P63/mmc) of WS₂ crystal for all the samples. All the parameters obtained

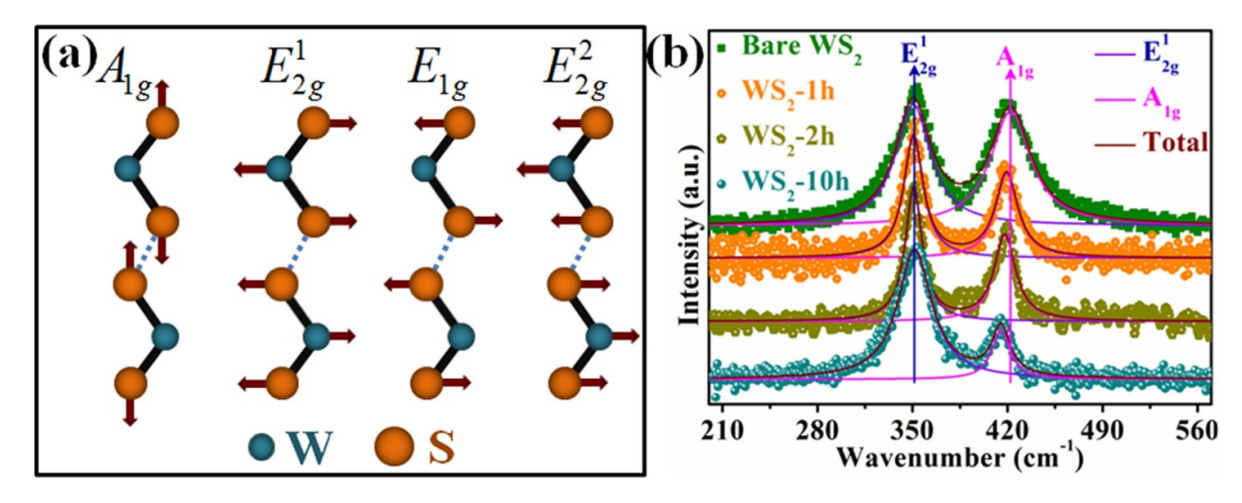


Figure 3. (a) Four major Raman active modes of WS₂. (b) Comparative peak positions of the E_{2g}^1 and A_{1g} mode of four samples (bare-WS₂, WS₂-1h, WS₂-2h and WS₂-10h).

Table 1. Raman peak positions, the difference between peak positions and the intensity ratio of the E_{2g}^1 and A_{1g} modes for the samples of bare-WS₂, WS₂-1h, WS₂-2h and WS₂-10h.

	Peak positions (cm ⁻¹)			
Samples	E_{2g}^1	A_{1g}	Difference (Δ) between peaks of E_{2g}^1 and E_{1g} (cm ⁻¹)	Intensity ratio $\left(I_{E_{2g}^1}\Big/I_{A_{1g}}\right)$
Bare-WS ₂	350.4	422.2	71.8	1.06
WS_2-1h	350.7	419.2	68.5	1.43
WS_2 -2h	350.8	417.9	67.1	1.55
WS_2-10	351.5	415.2	63.7	2.61

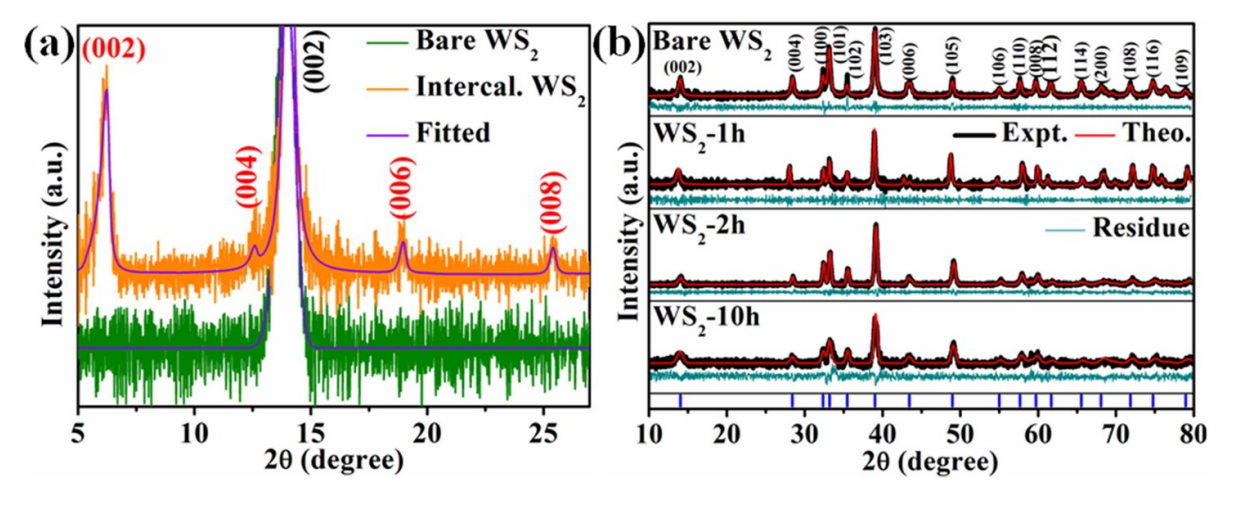


Figure 4. (a) Comparison of PXRD profiles for the intercalated WS_2 sheet with respect to the chemically synthesised bare- WS_2 sheet. (b) PXRD profiles for bare- WS_2 , WS_2 -1h, WS_2 -2h and WS_2 -10h samples.

from the Rietveld refinement are tabulated in table 2. As the electrolysis time increases, the relative intensity for the (002) set of planes decreases which indicates the decrease of layer numbers in the sheet. The relative intensity for the WS_2 -10h sample is the minimum which indicates the minimum number of layers in the WS_2 -10h sample (maximum time electrolysis sample). From this data we can conclude that, to get a sufficiently thin molecular-thick layer of WS_2 crystal, we have to perform the electrolysis process for a sufficient amount of time. If we observe the data for the root mean square (RMS) lattice strain, it shows that the value increases with the increase

of electrolysis-time and shows the sufficiently high value for the WS_2 -10h sample. The fairly high value of the crystallite size advocates the good crystallinity and sufficiently large crystal domain for all the samples.

3.4. Atomic force microscopy

The layer thickness (number of layers) of the exfoliated WS_2 sheet was measured from the AFM image, as shown in figure 5. The average thickness of the sheet for the bare-WS₂ sample is about 5.02 nm for an average lateral dimension of 880 nm

Lattice parameters (Å) Sample Crystalline phase c Average crystallite size (nm) RMS lattice strain Goodness of fit a 5.28×10^{-6} Bare-WS2 WS_2 3.18 ± 0.01 12.52 ± 0.01 926 1.63 3.80×10^{-4} WS_2-1h WS_2 3.17 ± 0.02 12.52 ± 0.02 361 1.26 9.22×10^{-4} WS_2-2h WS_2 3.17 ± 0.01 12.50 ± 0.01 230 1.12 3.16×10^{-3} WS2-10h WS_2 3.16 ± 0.01 12.46 ± 0.06 120 1.21

Table 2. Structural details obtained from PXRD data (Rietveld refinement).

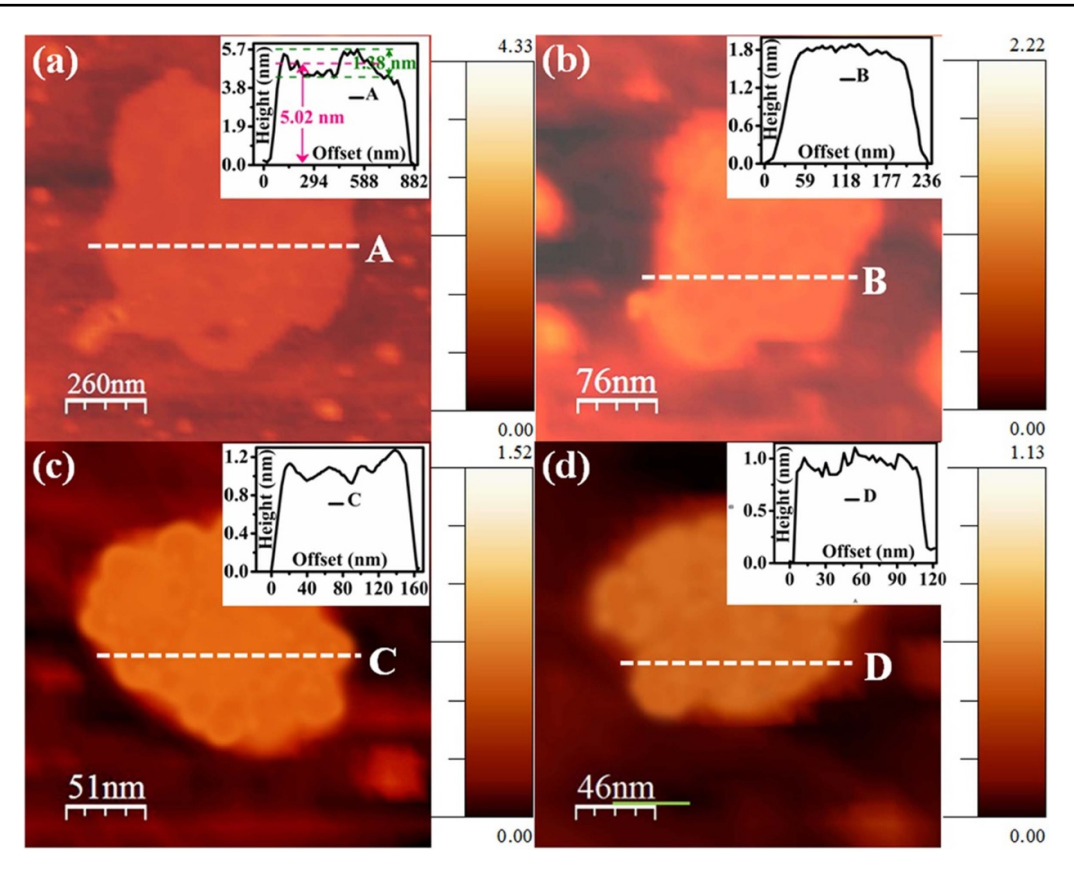


Figure 5. (a) AFM image for the bare-WS₂ sheet (inset shows height profile along A). (b) AFM image for the sample WS₂-1h (inset shows height profile along B). (c) AFM image for the sample WS₂-2h (inset shows height profile along C). (d) AFM image for the sample WS₂-10h (inset shows height profile along D).

(figure 5(a)). The thickness for the WS₂-1h, WS₂-2h and WS₂-10h samples are calculated as 1.8, 1.2 and 1.0 nm, respectively (figures 5(b) and (d)). From the TEM image analysis, it was calculated that the interlayer spacing between two adjacent layers of the WS₂ sheet was about 0.62 nm (see figure S3 in the supplementary material) [29]. Therefore, the average number of layers in the bare-WS₂, WS₂-1h, WS₂-2h and WS₂-10h is calculated as 8, 2, 2 and 1–2, respectively. This result is in good agreement with the Raman study of the samples.

3.5. X-ray photoelectron spectroscopy

Figure 6(a) shows the full range XPS spectrum for a typical exfoliated WS₂ sample. The spectrum contains only the peaks for W and S which confirms the phase purity of the WS₂ sheet. All the peaks are referenced with the shift of the standard C 1s spectrum, as shown in figure 6(b) [37]. Two peaks near 284.8 and 286.5 eV in the C 1s region correspond to the C–C bond

and C-O bond, respectively [38]. To know the exact peak positions, we took a slow scan of the W 4f and S 2p regions. The exact peak positions at 33.2, 35.1 and 38.8 eV, as shown in figure 6(c), obtained from the deconvolution, correspond to W $4f_{7/2}$, $4f_{5/2}$ and $5p_{3/2}$, respectively [39, 40]. The peak positions at 162.8, and 164.1 eV correspond to S 2p_{3/2} and 2p_{1/2}, respectively (figure 6(d)) [37, 38]. In comparison with the literature value of all the peak positions, it is found that the peaks corresponding to the W 4f spectra have shifted slightly towards lower values whereas the same for the S 2p spectra have shifted towards higher values. No peaks for other phases (1T or 3R-phase) indicate the phase purity of the 2H-phase of the WS₂. The ratio of the elemental percentage of WS₂ calculated from the XPS spectra using proper Scofield's relative sensitivity factor for each element is 1:1.87 instead of 1:2. This data indicates a significant amount of atomic vacancy in the S site of the exfoliated WS₂ crystal. The most interesting part to note is that there is no peak in the region (600–800 eV) corresponding

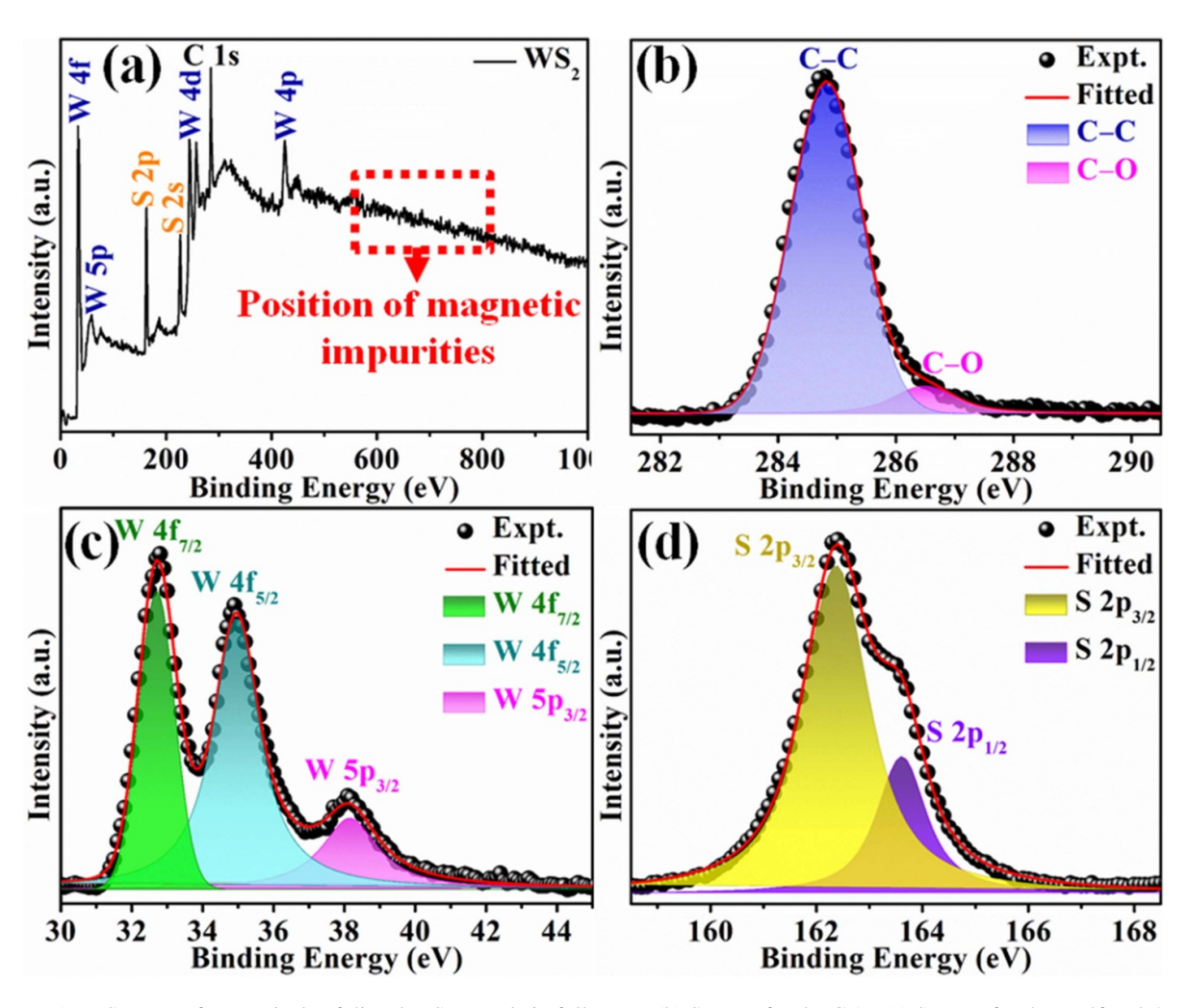


Figure 6. (a) XPS spectra for a typical exfoliated WS₂ sample in full range. (b) Spectra for the C 1s. (c) Spectra for the W 4f and 5p. (d) Spectra for S 2p.

Table 3. Curie constants from the Curie–Weiss $\left(\frac{1}{\chi}vs.T\right)$ plot.

	$\Theta\left(\mathbf{K}\right)$		$C (\times 10^{-6}) (emuKg^{-1}Oe^{-1})$	
Sample	Value	SD	Value	SD
WS ₂ -2h WS ₂ -10h	2.2 54.5	0.001 0.001	5.99 8.84	0.001 0.001

to magnetic elements (figure 6(a)). This indicates that the observed magnetic behaviour of the sample has not come from any undesired magnetic impurity [41, 42].

3.6. Magnetic data analysis

Pristine WS₂ crystal is diamagnetic in nature [43]. Figure 7(a) shows the susceptibility vs. temperature $(\chi(T))$ curve, in both the zero-field-cooled and field-cooled (ZFC-FC) mode, at an applied field of 100 Oe, for the sample WS₂-1h. The $\chi(T)$ shows a diamagnetic nature, whereas it shows paramagnetic like behaviour in the low-temperature region. We have fitted the $\chi(T)$ vs. T data using the Curie law $\chi(T)$ (inset of figure 7(a)). But the experimental data are not in agreement

with the theoretical data in the region above the temperature of 60 °C. In figure 7(b), the isothermal hysteresis curves, i.e. the magnetisation vs. applied field (M(H)) at different temperatures for the sample WS₂-1h, clearly show competition between a diamagnetic and a paramagnetic behaviour. In the low field region, it shows paramagnetic-like behaviour, whereas it tends to become diamagnetic as the applied field strength (H) increases. Figure 7(c) shows the $\chi(T)$ as a function of T (ZFC-FC) for the sample WS₂-2h. Throughout the whole temperature range (2–300 K), the $\chi(T)$ vs. T (ZFC-FC) shows paramagnetic nature. The inset of figure 7(c) shows the inverse susceptibility $\left(\frac{1}{\chi}\right)$ data as a function of T, which follows the linear Curie–Weiss law $\left(\frac{1}{\chi} = \frac{T}{C} - \frac{\Theta}{C}\right)$. The linear fit of the inverse susceptibility plot indicates that the WS2-2h sample is perfectly paramagnetic. No separation between $\chi(T)$ in the ZFC and FC mode indicates no coercivity in the M(H) plot. Curie constants obtained from the Curie-Weiss fitting are summarized in table 3. The M(H) data for the WS₂-2h sample, as shown in figure 7(d), show a paramagnetic behaviour with a saturation of magnetisation and zero coercivity. Figure 7(e) shows the $\chi(T)$ vs. T(ZFC-FC) data for the WS₂-10h sample. The susceptibility curves in the ZFC and

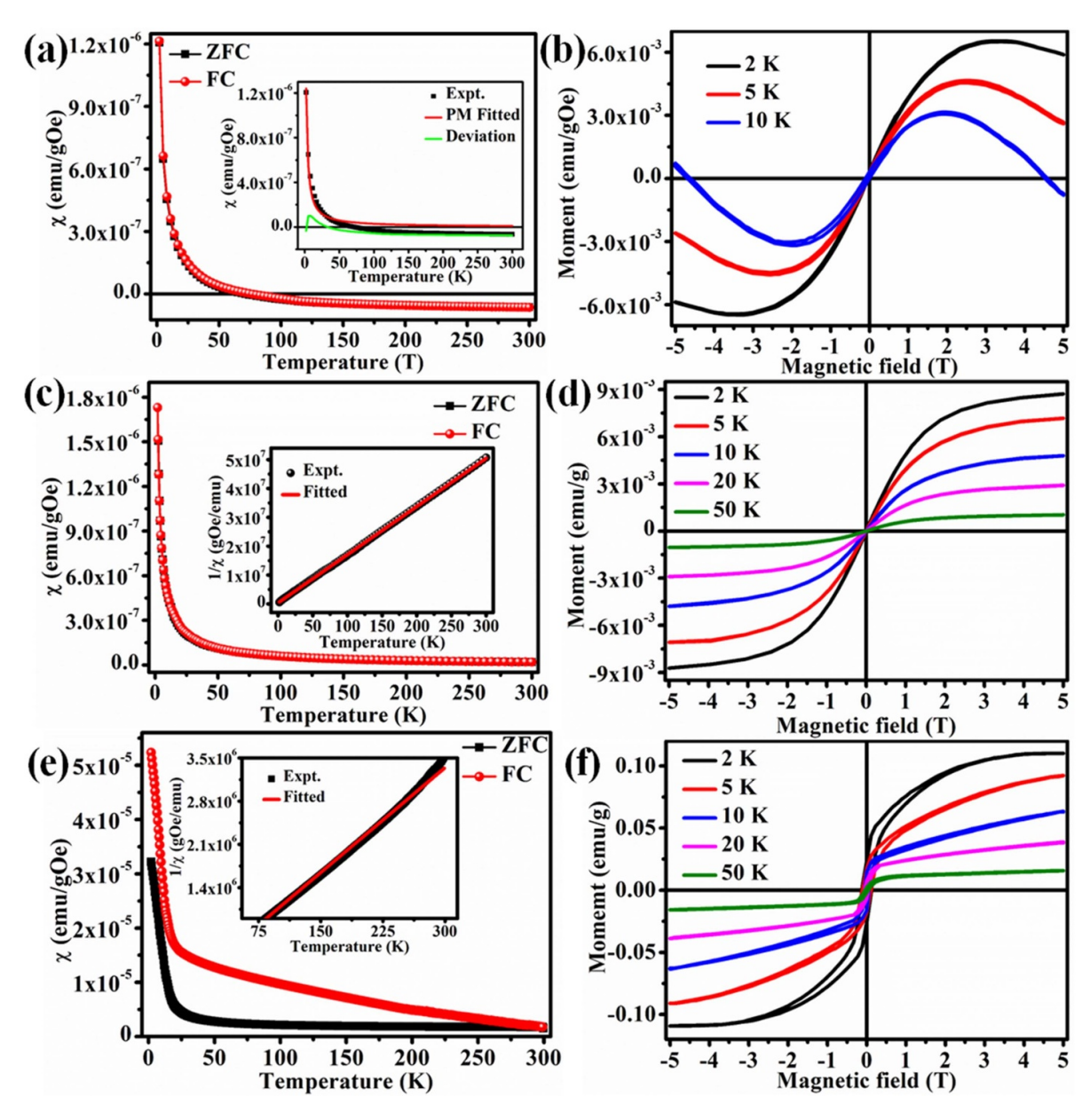


Figure 7. (a) $\chi(T)$ (ZFC-FC) for the WS2-1h sample, and the paramagnetic fit of $\chi(T)$ (ZFC) (inset). (b) M(H) for the sample WS2-1h. (c) $\chi(T)$ (ZFC-FC) for the WS2-2h sample, and Curie-Weiss fit of $1/\chi$ vs. T plot in ZFC mode (inset). (d) M(H) for the sample WS2-2h. (e) $\chi(T)$ (ZFC-FC) for the WS2-10h sample, and Curie-Weiss fit of $\frac{1}{\nu}$ vs. T plot in ZFC mode (inset). (f) M(H) for the sample WS2-10h.

FC mode show a bifurcation in the low-temperature region, which indicates an ordering of the magnetic moments within the system. The inset of figure 7(e) shows the Curie–Weiss fitting $\left(\frac{1}{\chi} = \frac{T}{C} - \frac{\Theta}{C}\right)$ of $\frac{1}{\chi}$ vs. T plot. Curie constants obtained from the fitting are summarized in table 3. The M(H) data for the WS₂-10h sample, as shown in figure 7(f), show a ferromagnetic ordering with fairly good coercivity (1227, 1109, 558, 501 and 438 Oe at 2, 5, 10, 20 and 50 K, respectively) and magnetic saturation. The coercivity data at different temperatures are summarised in table 4. Therefore, it is seen that the ordering for the WS₂-2h sample is better than the WS₂-1h sample, whereas the magnetic ordering in WS₂-10h is the best among all the samples. This means that, as the time for the electrochemical intercalation increases, the generation of the magnetic moment also increases and, as a result, the magnetic

Table 4. Comparison of coercivity values of WS_2 -10h at different temperatures.

Sample	Temperature (K)	Average coercivity (Oe)
WS ₂ -10h	2	1227
	5	1109
	10	558
	20	501
	50	438

ordering becomes good with the increase of the electrochemical intercalation time.

With the increase of electrochemical-intercalation time, the intercalation of the giant-molecules within the interlayer separation of the WS_2 crystal is greater, which results

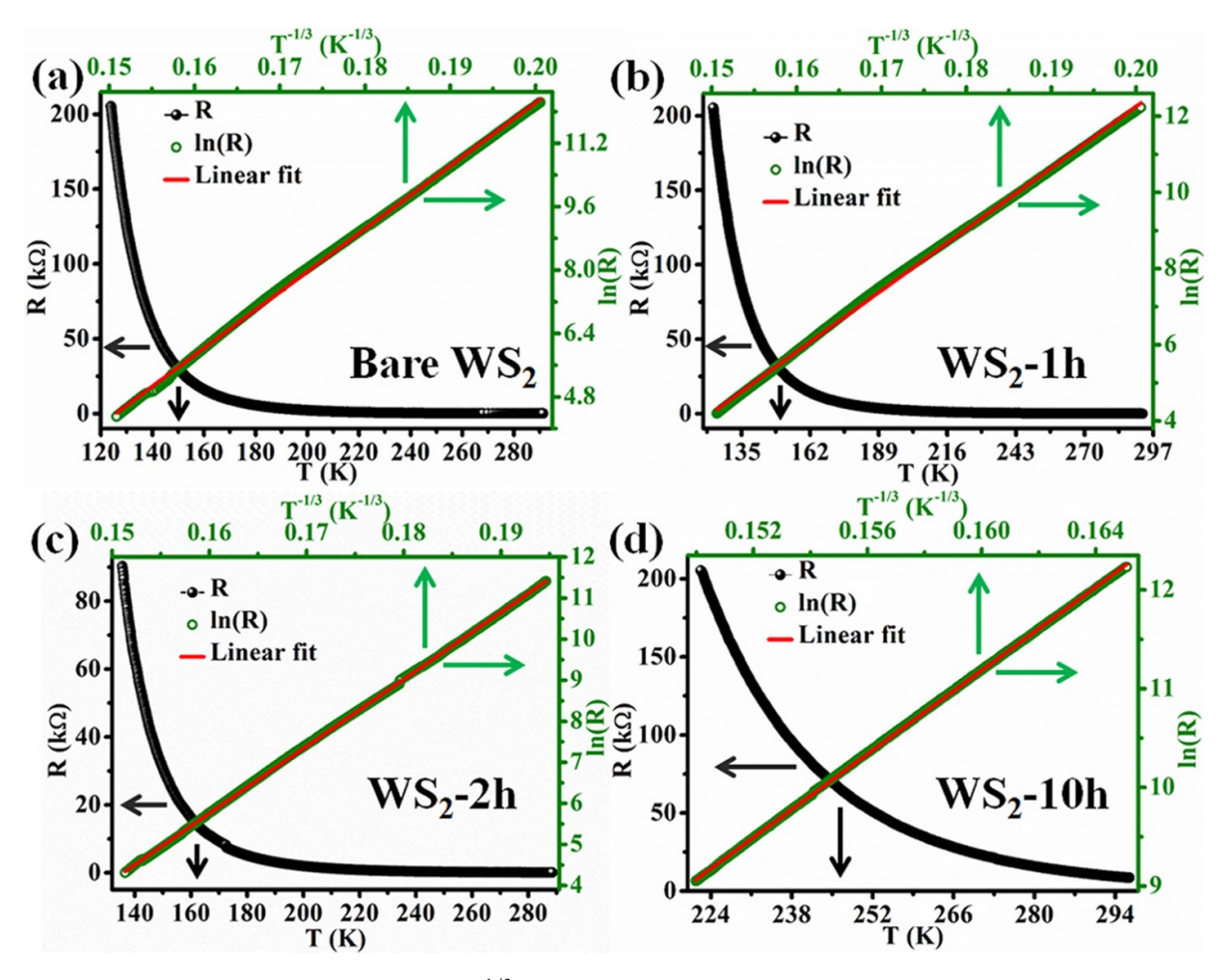


Figure 8. R(T) (black) and linear fitting of $\ln(R)$ vs. $T^{-1/3}$ (green) for the sample of (a) bare-WS₂, (b) WS₂-1h, (c) WS₂-2h and (d) WS₂-10h.

in better exfoliation of the sheet. The RMS lattice strain within the system calculated from the PXRD data (see the detail of the Rietveld refinement in the supplementary material) shows that the value increases with the increase in electrochemical-intercalation time, i.e. for the betterexfoliated sheet. TEM results also show that the structural defect arises within the exfoliated sheet. The elemental atomic percentage calculated from the EDXS data in TEM, and the XPS spectra, suggest that there is a significant number of S vacancies compared to W atoms in the as-exfoliated sheet. The reaction temperature is not as high as to create an antisite, thereby the possibility of creation of an antisite has been removed. As per the vacancy of the S atom over the W atom, we have also discarded the possibility of V_{3W} vacancies. Considering all the possibilities, we have concluded that V_{1W+2S} and V_{6S} are the most preferential atomic vacancy defects in our sample. The density functional theory calculation shows that the electronic energy levels in W and S sites near the vacancy defects have got redistributed [25, 44]. The energy levels due to the vacancy defect of W lies near the valence band maxima, whereas the same for the S lies near the conduction band minima [25, 44]. This redistribution of the electronic energy states attributes an imbalance in the spin majority and spin minority bands, owing to a net magnetisation. Near V_{1W+2S} and V_{6S} the spin-imbalance occurs especially within S 2p states and W d states. The spin moment near V_{1W+2S} is created due to the adjacent out-of-plane d_{xz/yz} state of W and the p_x and p_y state of S, whereas for V_{6S} the spin moment is created due to the adjacent out-of-plane d_z² states of W. The magnetic moment for the atomic vacancy defects V_{1W+2S} and V_{6S} are calculated as 0.981 and 0.608 μ_B , respectively, within the thin layer of the WS₂ sheet [25, 44]. Inevitably, the increase of electrochemical-intercalation time and hence the atomic vacancy defects, especially for V_{1W+2S} and V_{6S}, create a significant amount of magnetic moment and ordering of it for the higher time intercalated samples (WS2-2h and WS2-10h). If we observe the ZFC-FC data of the WS₂-10h sample (figure 7(e)), we can see a bifurcation even after the transition temperature. The reason behind this is the randomly oriented ultrafine magnetic domains. In the thin sheet of WS2, the magnetic moments arise from the vacancies. In a particular sheet, there are several ultrafine magnetic domains. The ultrafine magnetic domains are randomly oriented in the powdered sample used for magnetic measurements. This is why, instead of showing complete ferromagnetism (no bifurcation between FC and ZFC after the transition temperature), the system shows a spin-glass like behaviour (a small bifurcation in FC and ZFC after transition temperature).

Slope of logarithmic plot (K³) Characteristic temperature, $T_M(K)$ R^2 Value Sample Value Error Error 4.04×10^{6} 0.99 Bare-WS2 159.27 0.13 0.39 WS_2-1h 160.95 0.12 4.16×10^{6} 0.36 0.99 WS_2-2h 0.05 4.33×10^{6} 0.99 163.09 0.15 WS₂-10h 9.44×10^{6} 211.39 0.09 0.27 0.99

Table 5. Characteristic temperature (T_M) calculated from the logarithmic plot of resistance $(\ln(R) \text{ vs. } T^{-1/3} \text{ plot})$.

3.7. Transport study

It is seen from Mott's consideration of the variable range hopping (VRH) mechanism [45–47] that the resistivity (ρ) for a d-dimensional semiconducting crystal is of the form of

$$\rho(T) = \rho_0 \exp\left(\frac{T_M}{T}\right)^{\frac{1}{1+d}} \tag{1}$$

where ρ_0 is a temperature-dependent prefactor of the form of AT^m , and T_M is a characteristic temperature depending upon the density of states at Fermi level $(N(E_F))$ and the localisation radius (α) as

$$T_M = \frac{\beta}{k\alpha^3 N(E_F)}. (2)$$

 β is a numerical coefficient. Unlike the doped semiconducting system, in the pristine WS₂ sheet, where the estimated Coulomb gap $(\Delta_C \approx e^4 N(E_{\rm F}))$ between two interacting electrons is negligibly small (<1 mK), the density of states (N(E)) becomes constant near the Fermi level $(E_{\rm F})$ [48, 49]. The transport mechanism of the pristine WS₂ sheet can be described by the Mott-VRH equation for 2D (i.e. for d = 2) [50], given by,

$$\rho(T) = \rho_0 \exp\left(\frac{T_M}{T}\right)^{\frac{1}{3}}.$$
 (3)

To check the electron transport behaviour of the exfoliated WS₂ samples after the electrochemical exfoliation, we performed the transport measurements for all the exfoliated samples (WS₂-1h, WS₂-2h and WS₂-10h) along with the bare-WS₂ sample. Figure 8(a) shows the resistance vs. temperature (R(T)) plot for the bare-WS₂ sample, which shows a typical semiconducting nature. To understand the transport mechanism, we analysed the logarithmic plot of resistance ln(R) as a function of different powers of temperature (T). The dependency of the logarithmic resistance value (ln(R)) with respect to the $T^{-1/3}$ value shows a linearity (figure 8(a)) [48, 50]. All the exfoliated samples (WS2-1h, WS2-2h and WS2-10h) show a semiconducting nature and the logarithmic plot of resistance, ln(R), follows linear dependency on $T^{-1/3}$ (Mott-VRH) (figures 8(b) and (d)). From the slope of the logarithmic plot, the characteristic temperatures (T_M) of the Mott-VRH for all the samples have been calculated, which are summarised in table 5. The values of the adjusted R-square (R^2) for all the four fits are very close to unity. This indicates that the quality of fit is very good. As the localisation length (α) is inversely proportional to the cube root of characteristic temperature (T_M) , the values of α for all the samples, calculated from the value of T_M , are very low, which confirms the localisation of hopping electrons [47]. These results indicate that electron transport (semiconducting) behaviour has not been hampered due to the electrochemical-exfoliation of the WS₂ sheet.

4. Conclusion

In summary, this study has demonstrated a facile synthesis technique for a freestanding ultrathin WS₂ layer and the incorporation of ferromagnetism within it without changing its semiconducting behaviour. Using the reliance technique of electrochemical-exfoliation, a stable, unstacked and molecular-thick layer of WS₂ has been achieved. The intrinsic vacancy defects (especially V_{1W+2S} and V_{6S}) created in this synthesis-technique generate some amount of magnetic moment. There is an ordering of the as-generated moments resulting in ferromagnetic saturation and the system shows a soft-ferromagnetic behaviour. During this reliance process of exfoliation, the electrical property of the system has not been changed from its intrinsic semiconducting behaviour. At the end, in this way, a ferromagnetic semiconductor is achieved from a nonmagnetic 2D WS2 sheet which will be useful for spintronic devices. It is expected that this process will also be useful for achieving and tuning the magnetic properties of other 2D TMDs too.

Acknowledgements

A D acknowledges the Innovation in Science Pursuit for Inspired Research (INSPIRE) programme, Department of Science and Technology (DST), Government of India (GOI) for providing fellowship (IF160050). B K S acknowledges the Royal Society and the Science and Engineering Research Board (SERB) of GOI for providing the Newton International Fellowship (NIF\R1\180163). S K S acknowledges the DST, GOI and UGC-DAE CSR, Kolkata Centre.

ORCID iDs

Anup Debnath https://orcid.org/0000-0002-7308-9902 Bikash Kumar Shaw https://orcid.org/0000-0003-3249-2487

Shatabda Bhattacharya https://orcid.org/0000-0001-5401-6962

Shyamal K Saha https://orcid.org/0000-0002-6302-9105

References

- [1] Wang Q H, Zadeh K K, Kis A, Coleman J N and Strano M S 2012 Nat. Nanotechnol. 7 699–712
- [2] McCormick E J, Newburger M J, Luo Y K, McCreary K M, Singh S, Martin I B, Cichewicz E J Jr, Jonker B T and Kawakami R K 2018 2D Mater. 5 011010
- [3] Ahn E C 2020 npj 2D Mater. Appl. 4 17
- [4] Liu K K et al 2012 Nano Lett. 12 1538-44
- [5] Mak K F, Lee C, Hone J, Shan J and Heinz T F 2010 Phys. Rev. Lett. 105 136805
- [6] Eda G, Yamaguchi H, Voiry D, Fujita T, Chen M and Chhowalla M 2011 Nano Lett. 11 5111–16
- [7] Lauritsen J V, Kibsgaard J, Helveg S, Topsøe H, Clausen B S, Lægsgaard E and Besenbacher F 2007 Nat. Nanotechnol. 2 53–8
- [8] Lee Y H et al 2012 Adv. Mater. 24 2320-5
- [9] Rapoport L, Bilik Y, Feldman Y, Homyonfer M, Cohen S R and Tenne R 1997 Nature 387 791–3
- [10] Remškar M, Škraba Z, Regula M, Ballif C, Sanjinés R and Lévy F 1998 Adv. Mater. 10 246–9
- [11] Zhu Y Q, Hsu W K, Firth S, Terrones M, Clark R J H, Kroto H W and Walton D R M 2001 Chem. Phys. Lett. 342 15–21
- [12] Novoselov K S, Jiang D, Schedin F, Booth T J, Khotkevich V V, Morozov S V and Geim A K 2005 Proc. Natl Acad. Sci. USA 102 10451–3
- [13] Voiry D, Mohite A and Chhowalla M 2015 Chem. Soc. Rev. 44 2702–12
- [14] Voiry D et al 2013 Nat. Mater. 12 850-5
- [15] Mahler B, Hoepfner V, Liao K and Ozin G A 2014 J. Am. Chem. Soc. 136 14121–7
- [16] Debnath A, Bhattacharya S and Saha S K 2020 J. Phys. D: Appl. Phys. 53 225004
- [17] Lin Z et al 2018 Nature **562** 254–8
- [18] Wang C et al 2018 Nature 555 231-6
- [19] Žutić I, Fabian J and Sarma S D 2004 Rev. Mod. Phys. 76 323–410
- [20] Ataca C, Soahin H and Ciraci S 2012 J. Phys. Chem. C 116 8983–99
- [21] Zheng H, Yang B, Wang D, Han R, Du X and Yan Y 2014 Appl. Phys. Lett. 104 132403
- [22] Cai L et al 2015 J. Am. Chem. Soc. 137 2622–7
- [23] Hong J et al 2015 Nat. Commun. 6 6293
- [24] Wang S, Robertson A and Warner J H 2018 Chem. Soc. Rev. 47 6764
- [25] Zhao X, Dai X, Xia C and Wang T 2015 Superlattices Microstruct. 85 339–47

- [26] Ataca C and Ciraci S 2011 J. Phys. Chem. C 115 13303-11
- [27] Zhao G, Han S, Wang A, Wu Y, Zhao M, Wang Z and Hao X 2015 Adv. Funct. Mater. 25 5292–9
- [28] Sang Y, Zhao Z, Zhao M, Hao P, Leng Y and Liu H 2015 *Adv. Mater.* **27** 363–9
- [29] Rout C S, Joshi P D, Kashid R V, Joag D S, More M A, Simbeck A J, Washington M, Nayak S K and Late D J 2013 Sci. Rep. 3 3282
- [30] Wang F, Kinloch I A, Wolverson D, Tenne R, Zak A, O'Connell E, Bangertand U and Young R J 2016 2D Mater. 4 015007
- [31] Zeng H et al 2013 Sci. Rep. 3 1608
- [32] Guo Y et al 2018 Sci. Adv. 4 6252
- [33] Rietveld H W 1969 J. Appl. Cryst. 2 65
- [34] Debnath A, Bhattacharya S, Mondal T K, Tada H and Saha S K 2020 *J. Appl. Phys.* **127** 013901
- [35] Debnath A, Bhattacharya S and Saha S K 2017 Phys. Rev. B 96 214433
- [36] Zheng J, Zhang H, Dong S, Liu Y, Nai C T, Shin H S, Jeong H Y, Liu B and Loh K P 2014 Nat. Commun. 5 2005
- [37] Beamson G and Briggs D 1992 High Resolution XPS of Organic Polymers: The Scienta ESCA300 Database (New York: Wiley)
- [38] Jurkiewicz K, Hawełek Ł, Balin K, Szade J, Braghiroli F L, Fierro V, Celzard A and Burian A 2015 J. Phys. Chem. A 119 8692–701
- [39] Pagona G, Bittencourt C, Arenal R and Tagmatarchis N 2015 Chem. Commun. 51 12950
- [40] Park J, Kim M S, Cha E, Kim J and Choi W 2017 Sci. Rep. 7 16121
- [41] Tongay S, Varnoosfaderani S S, Appleton B R, Wu J and Hebard A F 2012 Appl. Phys. Lett. 101 123105
- [42] Yang Z, Gao D, Zhang J, Xu Q, Shi S, Tao K and Xue D 2015 Nanoscale 7 650–8
- [43] Luxa J, Jankovský O, Sedmidubský D, Medlín R, Maryško M, Pumerad M and Sofer Z 2016 Nanoscale 8 1960
- [44] Li W F, Fang C and Huis M A V 2016 Phys. Rev. B 94 195425
- [45] Mott N F 1968 J. Non Cryst. Solids 1 1
- [46] Mott N F, Pepper M, Pollitt S, Wallis R H and Adkins C J 1975 Proc. R. Soc. A 345 169
- [47] Shklovskii B I and Efros A L 1984 Electronic Properties of Doped Semiconductors (Berlin: Springer) pp 202–4
- [48] Kim J S et al 2016 ACS Nano 10 7500-6
- [49] Keuls F W V, Hu X L, Jiang H W and Dahm A J 1997 Phys. Rev. B 56 1161–19
- [50] Ovchinnikov D, Allain A, Huang Y S, Dumcenco D and Kis A 2014 ACS Nano 8 8174–81